RSC Advances

PAPER

View Article Online
View Journal | View Issue

Cite this: *RSC Adv.*, 2026, **16**, 15569

MWCNT-Au/Pt-modified screen-printed electrode for electrochemical detection of secondary metabolites in *Ganoderma*-infected oil palms

Arda Fridua Putra,[a] Fadlilatul Taufany,[b] Rio Akbar Yuwono,[cd] Chusnul Khotimah,[cd] Fu-Ming Wang,[cd] Chi-Hsien Huang[ae] and Ruri Agung Wahyuono *[af]

Ganoderma boninense infection affects nearly half of Indonesia's palm oil plantations, which leads to severe economic losses. Conventional detection methods like PCR are limited by cost and complexity, while electrochemical detection offers a promising alternative by targeting plant-derived metabolites. This study focuses on developing a low-cost, custom fabricated screen-printed electrode (SPE) modified with MWCNTs and Au/Pt nanoparticles to enable practical, scalable early detection of *G. boninense* in oil palm plantations using various electrochemical techniques. The SPE was fabricated using conductive carbon ink on sticker paper and modified with MWCNT-Au/Pt nanocomposites to enhance performance. Pt nanoparticles (2.5, 5, and 10 mM) were synthesized hydrothermally, while Au (5 mM) was prepared *via* citrate reduction. The nanocomposites were formed by sonication and applied *via* drop-casting. Characterization was performed using UV-vis, FTIR, XPS, SEM, contact angle, four-point probe, CV, and EIS. Electrochemical detection of phytol, quinoline, and stigmasterol was conducted using DPV and chronoamperometry in phosphate buffer saline. The results indicate that surface modification enhances conductivity and hydrophilicity, improving the charge transfer process in electrochemical detection. The best combination for SPE modification was the 3 : 1 ratio and 5 mM Pt concentration. The best detection results using DPV were achieved for phytol, quinoline, and stigmasterol, with respective R^2 and LOD of 0.98 and 2.85 mM, 0.95 and 2.36 μM, and 0.98 and 1.36 μM. Repeated testing on the SPE demonstrated good stability, despite being designed as a disposable test kit. Further, the SPEs demonstrate low detection limits and high sensitivity, highlighting their potential for early diagnosis and rapid screening of *Ganoderma*-infected oil palm trees as an accessible alternative for disease prevention.

Received 22nd December 2025
Accepted 10th February 2026

DOI: 10.1039/d5ra09886f

rsc.li/rsc-advances

Introduction

Indonesia and Malaysia are the leading producers of palm oil, contributing approximately 84% of global output. However, this high production is accompanied by significant economic losses, estimated at up to USD 500 million annually, due to infection by the pathogenic fungus *Ganoderma boninense*.[1–3] This species is particularly aggressive and transmissible compared to other *Ganoderma* species. Infected young oil palm trees typically die within 6–24 months after the onset of symptoms, while older trees may survive for 2–3 years.[4] In Indonesia, it is estimated that up to 45% of oil palm plantations have been affected, primarily through root contact with infected stem and root residues.[5,6] Therefore, early detection is essential as visible symptoms often do not appear until the infection has progressed to approximately 60–70%.[6]

Several detection methods have been developed, including laboratory-based techniques such as polymerase chain reaction (PCR) and immunoassays.[3,7,8] However, their application is limited due to high equipment costs, procedural complexity, and the requirement for skilled personnel. As an alternative, electrochemical detection offers a more accessible approach with advantages including lower cost, portability, and simplified instrumentation.[9–11] This technique can be deployed to detect secondary metabolites produced by oil palm trees as part of their defence response to *G. boninense*, *e.g.*, α-tocopherol, phytol, stigmasterol, and quinoline.[12,13] Phytol, a diterpene alcohol released during chlorophyll degradation, has been shown to be a potential indicator of plant stress and disease

[a]*Department of Engineering Physics, Institut Teknologi Sepuluh Nopember, Surabaya 60111, Indonesia. E-mail: wahyuono@its.ac.id*

[b]*Department of Chemical Engineering, Institut Teknologi Sepuluh Nopember, Surabaya 60111, Indonesia*

[c]*Graduate Institute of Applied Science and Technology, National Taiwan University of Science and Technology, Taipei 10607, Taiwan*

[d]*Graduate Institute of Energy and Sustainability Technology, National Taiwan University of Science and Technology, Taipei 10607, Taiwan*

[e]*Department of Materials Engineering, Ming Chi University of Technology, New Taipei City 243303, Taiwan*

[f]*Graduate Program of Innovation in System and Technology, School of Interdisciplinary Management and Technology, Institut Teknologi Sepuluh Nopember, Surabaya 60264, Indonesia*

progression. Its concentration is closely associated with chlorophyll breakdown and can therefore reflect the severity of infection, particularly at advanced stages when leaf physiology is affected.[13,14] Despite its relevance, electrochemical detection of phytol has not been widely reported. In addition, quinoline and stigmasterol have been individually correlated with *Ganoderma boninense* infection in oil palm, however, studies addressing their simultaneous electrochemical determination in real plant matrices are still scarce. These gaps highlight the need for a multi-analyte sensing approach capable of monitoring phytol alongside established biomarkers to improve the assessment of *G. boninense* infection.

In recent years, screen-printed carbon electrodes (SPEs) have been widely developed for electrochemical sensors due to their disposability, portability, and low fabrication cost.[15–17] The performance of SPEs can be enhanced through surface modification using nanocomposites.[13,17,18] Carbon-based nanomaterials such as multi-walled carbon nanotubes (MWCNTs) and reduced graphene oxide (rGO) are commonly used for their high surface area, electrical conductivity, and the ability to support nanoparticle immobilization.[17,19,20] Compared with other carbon allotropes, MWCNTs exhibit higher stability and a larger surface area, which enhances charge-transfer performance and makes them widely used as electrode layers to facilitate electron transport.[19] MWCNTs can also be activated using oxidizing agents, improving their electrochemical properties by introducing functional groups such as –OH and –COOH that enable binding with other compounds or reagents.[21–23] Metal nanoparticles, including gold (Au), silver (Ag), and platinum (Pt), are frequently incorporated to carbon-based matrix to improve electrocatalytic activity. Gold nanoparticles are known for their high conductivity, biocompatibility, and redox properties, while platinum nanoparticles exhibit better electrocatalytic efficiency.[11,24–27] Despite their favourable properties, Pt-based nanocomposites have not been extensively investigated in the context of palm oil disease detection.

In addition to detection performance, fabrication simplicity and practical usability are important considerations for SPE development as rapid test devices. Electrochemical methods such as cyclic voltammetry (CV), differential pulse voltammetry (DPV), and linear sweep voltammetry (LSV) have been utilized in similar diagnostic applications.[13,22,28] However, many prior studies employed commercial SPEs modified *via* electrodeposition, a method that, while effective, is less suitable for mass production.[16,17] Therefore, alternative modification techniques such as drop-casting should be evaluated for their practicality and scalability.

This study aims to develop a low-cost, custom fabricated SPE modified with MWCNTs and Au/Pt nanoparticles for the electrochemical detection of *G. boninense* infection through analysis of secondary metabolites. Additionally, the study compares different electrochemical techniques to evaluate their potential for practical, rapid detection applications. This study also showcases the validation of custom fabricated SPEs modified with MWCNT-Au/Pt nanocomposite for rapid and cost-effective detection of *G. boninense*-infected oil palm tree for the first time.

Method

Materials and components

SPE fabrication requires transparent glossy sticker paper and PET film as the substrate, both purchased from local supplier, carbon paste (ρ = 1.05 g mL^{-1}) as the base electrode material obtained from MG Chemicals (Canada), and silver–silver/chloride (Ag/AgCl) paste (ρ = 2.83 g mL^{-1}) as the reference electrode material obtained from Merck (Germany). The catalyst precursors consist of –COOH functionalized multi-walled carbon nanotubes (MWCNT) purchased from Ossila (UK), hexachloroplatinic acid (H_2PtCl_6) purchased from SmartLab (Indonesia), gold chloride ($HAuCl_4$) purchased form Merck (Germany). Other chemicals used in nanoparticle synthesis are tri-sodium citrate dihydrate, iron(III) acetylacetonate ($Fe(acac)_3$), sodium chloride (NaCl), ethylene glycol (EG), all purchased from Merck (Germany), potassium iodide (KI) purchased from Merck (Germany), and polyvinylpyrrolidone 30 000 (PVP K30) purchased from BASF (Germany).

Secondary metabolite biomarkers of stigmasterol, quinoline, and phytol were purchased from Merck (Germany). Healthy and infected palm leaves sample were obtained from private palm oil plantation in Pemali District, Bangka Island, Indonesia. Whatman no. 1 filter papers were obtained from local supplier. Methanol and ethanol were purchased from Merck (Germany). Cold Spring Harbor protocol was used as reference to prepare 1× phosphate buffer saline (1× PBS) using sodium chloride (NaCl), potassium chloride (KCl), potassium dihydrogen phosphate (KH_2PO_4), and disodium hydrogen phosphate (Na_2HPO_4), all purchased from Merck (Germany). Methylene blue trihydrate ($C_{16}H_{18}ClN_3S\cdot 3H_2O$) for electrochemical analysis were also purchased from Merck (Germany). All the chemicals were analytical grade without further purification. Ultra-pure deionized water purchased from local supplier was used for synthesis.

Synthesis of MWCNT-Au/Pt

Au nanoparticles (Au NPs) were prepared by adapting a previously reported polyol-assisted synthesis method originally developed for Ag,[29] with modifications that included using citrate as the reducing agent.[30] 5 mM of $HAuCl_4$ precursor solution were prepared in 6 mL EG. The reducing agent was 0.34 M tri-sodium citrate in 3 mL of EG. The stabilizing agent for Au NPs synthesis was prepared using 96 mg PVP, 1 mg NaCl, and 1 mg $Fe(acac)_3$ in 6 mL of EG. All of the precursors, reducing agent, and stabilizing agent were added in 10 mL pre-heated EG at 160 °C. The mixture was then stirred for 2 minutes and then cooled down into room temperature.

Pt nanoparticles (Pt NPs) were synthesized hydrothermally using H_2PtCl_6 as the precursor.[31] H_2PtCl_6 varied from 2.5 to 10 mM and was mixed with KI in a mole's ratio of 1 : 4. Subsequently, 4.5 grams of PVP were added as the capping agent in 10 mL of distilled water. The solution was then heated in Teflon-lined autoclave at 180 °C for 90 minutes. Both the Au and Pt suspensions were centrifuged at 6000 rpm for 60 minutes, washed with ethanol, dried, and then redispersed in 5 mL of distilled water. The Au and Pt suspensions were subsequently

combined at a 1 : 1 (v/v) to form an Au/Pt mixture. Subsequently, a 1.2 mg mL^{-1} MWCNT suspension was prepared using a DI water–methanol solvent mixture (7 : 3, v/v), followed by sonication for 5 minutes. Au/Pt mixture were added into the MWCNT suspension at MWCNT to Au/Pt ratios of 6 : 1, 5 : 1, 4 : 1, and 3 : 1. The resulting mixtures were sonicated for 2 hours at room temperature to obtain MWCNT-Au/Pt. The synthesized Pt NPs were labelled as Pt *Y*, where $Y = 25$, 50, and 100 correspond to Pt precursor concentrations of 2.5, 5.0, and 10.0 mM, respectively. The synthesized nanocomposites were labelled as *X*/*Y*, where *X* represents the volume ratio of MWCNT to Au/Pt, and *Y* (25, 50, 100) indicates the Pt precursor concentration (2.5, 5.0, and 10.0 mM).

Fabrication of screen-printed electrode

Transparent glossy sticker papers used as media for SPE were peeled and attached to PET film. The sticker side of the film was then washed with ethanol. Subsequently copper tape was added. The SPE pattern, following the design of the previous study, with the modification of working electrode diameter into 0.4 cm and electrode length into 3 cm as seen in Fig. 1, was cut using a Jinka YS-360 sticker cutting machine.[32] To assist with the deposition of carbon ink *via* the doctor blade method, 2 mm tapes were placed on both edges of the film. The film was then cured in an oven at 120 °C for 30 minutes. The reference electrode pattern was then applied, with Ag/AgCl ink deposited using the same doctor blade technique, followed by another heating step at 120 °C for 20 minutes. Unnecessary parts of the SPE were removed using tweezers. For modification, 10 μL of MWCNT-Au/Pt suspension was drop-casted onto the working electrode area and then the SPE was heated at 120 °C for 15 minutes.

Characterization

FTIR with attenuated total reflection add-on JASCO 6700 were carried out to study the functional group of Au, Pt, and MWCNT-Au/Pt through infrared spectra. UV-vis absorption spectra of Au, Pt, and MWCNT-Au/were collected using ThermoScientific Genesys 150. X-Ray Photoelectron Spectroscopy (XPS) were also conducted using PHI 5000 VersaProbe III with a monochromated Al-Kα source. JEOL JSM-6500F Field Emission Scanning Electron Microscope (FESEM) was carried out to study surface morphology of SPE. Transmission Electron Microscope (TEM) and Energy Dispersive X-Ray (EDX) were carried out using Philips Tecnai F20 G2 FEI-SEM. Resistivity and conductivity of SPE surface were assessed using Four Point Probe (Ossila). Surface roughness of the SPE were analyzed from digital microscope images using open-sourced image processing tool ImageJ. Electrochemical measurements were performed using EmStat4S HR potentiostat and PSTrace 5.11 software from PalmSens with 1× PBS pH 7.4 as the supporting electrolyte. Cyclic voltammetry scans were conducted using methylene blue solution within the potential range of −1 to +1 V with scan rate of 100 mV s^{-1} and accumulation time of 10 seconds. Electrochemical Impedance Spectroscopy (EIS) was carried out within frequency of 0.1 Hz–100 kHz under 0.01 V open circuit condition.

Detection of secondary metabolites

Given the limited water solubility of the secondary metabolites, stock solutions of 150 mM phytol, 1.5 mM quinoline, and 1.5 mM stigmasterol were prepared in 0.1 M of methanol. The resulting stock solutions were stored at 14 °C until required for further use. To achieve the desired concentration, the stock solution was diluted using 1× PBS. For electrochemical detection the concentration range of phytol within 0.005–50 mM, quinoline within 0.1–200 μM, and stigmasterol within 0.1–200 μM were used. Detections were performed using Differential Pulse Voltammetry (DPV) within the potential range of −0.8 V to +0.6 V with scan rate of 0.025 V s^{-1}. Detections were also performed using chronoamperometry (CA) with E_{dc} of 1.0 V, time interval of 0.05 s, equilibration time of 10 s, and running time of 90 s.

The obtained results were then used to obtain calibration curve along the sensing performance parameter, *i.e.*, sensitivity which obtained from the slope of the calibration curve, repeatability which obtained from averaging the relative standard deviation (RSD) of six measurement replicates across all concentrations, limit of detection (LOD), and limit of quantification (LOQ). RSD were calculated as follows:

$$\mathrm{RSD} = \frac{\mathrm{SD}}{\bar{x}} \times 100\%$$

where SD is the standard deviation and $\bar{x}$ is the mean. LOD and LOQ were calculated using the following equation:

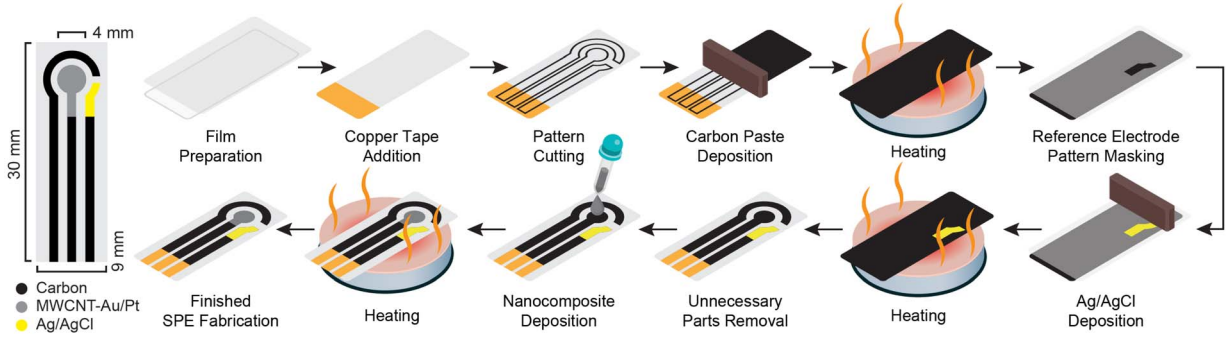

Fig. 1 Schematic design and fabrication steps of SPE.

$$\mathrm{LOD} = 3.3\left(\frac{S}{b}\right)$$

$$\mathrm{LOQ} = 10\left(\frac{S}{b}\right)$$

where S is the standard deviation of the y-residuals and y-intercepts of the linear regression line, and b is the slope of the calibration curve.

Evaluation of multi-analyte detection

The potential of the fabricated SPEs for simultaneous detection of multiple analytes was evaluated using multivariate analysis and interference studies. Principal component analysis (PCA) was employed to assess selectivity, while linear discriminant analysis (LDA) was used to evaluate specificity. PCA was performed using Python-based scripts on datasets consisting of peak current and peak potentials obtained from DPV measurements of individual metabolites. Subsequently, LDA classification was conducted using the same features with 5-fold stratified cross-validation to assess classification performance. Interference tests were carried out by recording DPV responses of binary mixtures of the metabolites, each at a concentration of 50 μM, to validate the selectivity and specificity of the SPEs under simultaneous detection conditions.

Detection of palm leaves extracts

The performance of the SPEs in real samples was evaluated using the standard addition recovery method. Two healthy and two infected oil palm leaf samples were dried in a vacuum oven at 45 °C for three days, cut into small pieces, and ground into fine powder. 200 mg of powder of each sample was dissolved in 400 mL of 80% methanol, followed by sonication for 30 minutes at room temperature. The mixture was filtered using Whatman filter paper, and the filtrate was centrifuged to collect the solid residue. The residue was dried and redispersed in 0.1 M methanol prepared in 1× PBS to obtain a leaf extract solution with a final concentration of 10 mg mL^{-1}.

A sample of 10 mL of each extract was first analyzed by DPV. The extracts were then spiked individually with phytol, quinoline, and stigmasterol at two concentration levels (high and low) by adding the metabolite directly followed by thorough mixing. The high-level spikes were 20 mM phytol, 80 μM quinoline, and 50 μM stigmasterol, while the low-level spikes were 6 mM phytol, 20 μM quinoline, and 20 μM stigmasterol. The spiked extracts were subsequently reanalyzed using the same DPV procedure as the previous metabolite test. The obtained results were then used to calculate the percentage recovery of each metabolite. Each sample was repeated three times.

Results and discussion

Characterization of MWCNT-Au/Pt

The FTIR spectra in Fig. 2(a) reveal distinct absorption peaks for the synthesized nanoparticles. Au NPs exhibit peaks at 1726, 1446, 1236, 1151, and 1070 cm^{-1}, while Pt NPs exhibit peaks at 1669, 1422, and 1285 cm^{-1}. As metallic bonds are IR-inactive, no direct metal-related bands are observed. The formation of Au and Pt NPs is indirectly supported by the presence of ligand-related vibrations and ligand–metal interactions on the nanoparticle surface. These absorption features are attributed to the capping and reducing agents used during nanoparticle synthesis, such as PVP and trisodium citrate, and correspond to their characteristic functional group vibrations. This interpretation is consistent with the previous report, where the presence of nanoparticles was confirmed using complementary techniques.[31] MWCNT used as the nanocomposite precursor exhibit several sharp peaks attributed to C–H, C–O, and O–H functional groups at 1024, 1081, 1156, 1217, 1349, and 1453 cm^{-1}. MWCNT also shows a C=C stretching peak around 1670 cm^{-1}.[33] A notable peak at 1536 cm^{-1}, associated with C=C–C stretching, further confirms the prominent characteristic of MWCNTs.[34,35] Upon formation of the MWCNT-Au/Pt nanocomposites, a noticeable decrease in absorbance at 1536 cm^{-1} is observed, indicating the disassociation of C=C–C bonds and subsequent interaction with either Au or Pt NPs.[31] In addition, the spectra show a trend of increasing absorbance at the characteristic Au

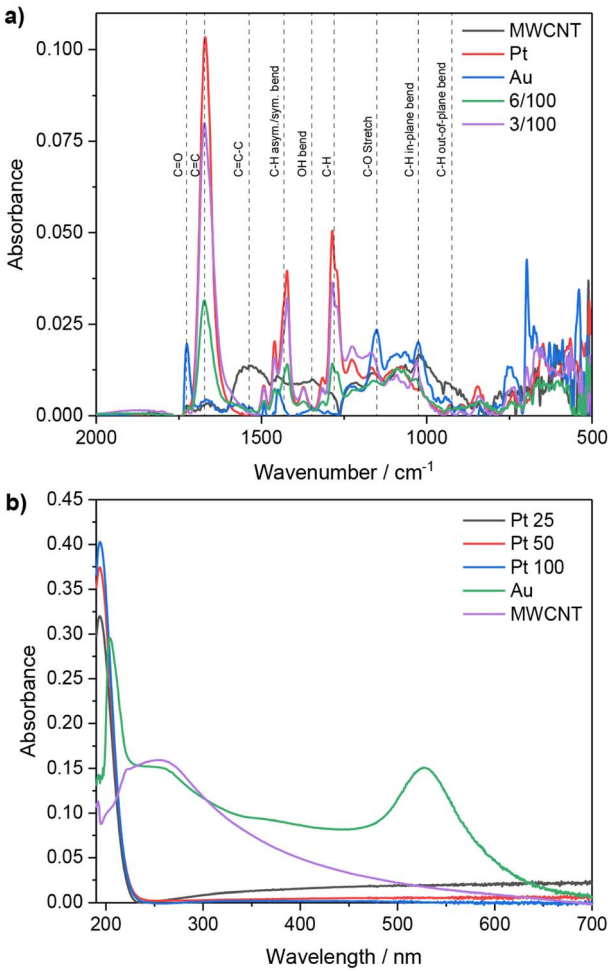

Fig. 2 (a) FTIR and (b) UV-vis absorbance spectra of MWCNT and synthesized Pt NPs, Au NPs, and MWCNT-Au/Pt.

and Pt peak positions as the volume ratio of MWCNT to Au/Pt decreased, suggesting higher nanoparticle interactions with the MWCNT.

The electronic properties of the synthesized nanoparticles are further confirmed using UV-vis absorption spectroscopy, as presented in Fig. 2(b). The absorbance spectrum reveals distinct peaks corresponding to each type of nanoparticle. MWCNT shows a peak at around 265 nm, while Pt NPs exhibit a characteristic absorption peak at 198.5 nm which appears as absorption shoulder. Absorption spectrum of Au NPs shows prominent peaks at 204 nm and 527 nm, along with a shoulder at 257 nm. These spectral features are consistent with previous reports, confirming the successful synthesis of the respective nanoparticles.[36–39]

The UV-vis absorption spectrum of the MWCNT-Au/Pt nanocomposites is presented in Fig. 3. A trend consistent with the FTIR findings is observed in Fig. 3(a), where increasing Au content leads to an increase of absorbance at 527 nm, while the characteristic MWCNT peak at 265 nm shows a decrease in intensity as the volume ratio of MWCNT to Au/Pt decreases. The absorbance peak observed at 265 nm corresponds to π–π^* electronic transitions associated with carbon bonding.[40] In comparison between the various MWCNT ratios, a high difference of absorbance between 5/25 and 4/25 compared to the 4/25 to 3/25 is present which may be due to the agglomeration of Au/Pt on MWCNT surface.

Similarly, Fig. 3(b) shows that an increase in Pt concentration is accompanied by an increase in absorbance at ~198 nm. The consistent peak position at this wavelength, without any observable shift, suggests a uniform particle size distribution, indicating that PVP effectively functioned as a capping agent to control the size of the Pt nanoparticles. However, a prominent peak appears at ~215 nm, particularly at higher Pt concentrations. This absorbance at 215 nm is likely attributed to residual PVP encapsulating NPs from the synthesis process.[41,42] The observed redshift and increase in intensity at this wavelength further support the presence of higher residual PVP at higher Pt concentrations due to the increase of Pt NPs.

Formation of MWCNT-Au/Pt nanocomposite is further examined by EDX elemental mapping, as shown in Fig. 3(c). The EDX maps confirm the presence of carbon (C), gold (Au), and platinum (Pt) within the composite, with carbon forming the continuous matrix and Au and Pt appearing as finely dispersed features across the MWCNT surface. The relatively uniform spatial distribution of Au and Pt indicates successful deposition of both metals onto the MWCNTs without pronounced phase segregation.

Quantitative EDX analysis shows atomic contributions of approximately 10.34% for Pt and 9.13% for Au, supporting the formation of a bimetallic nanocomposite. The comparable particle sizes of Au (0.76 nm) and Pt (0.68 nm) further suggest controlled nucleation and growth during synthesis, consistent

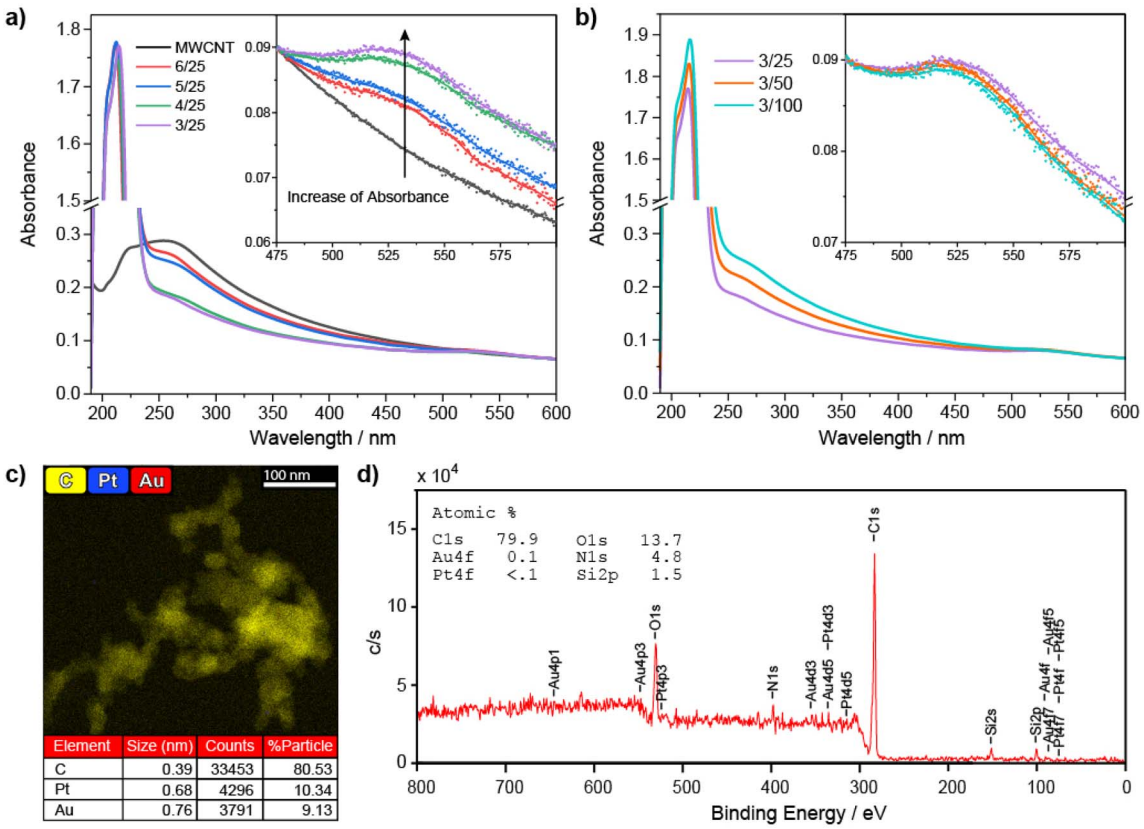

Fig. 3 UV-vis absorption spectra of various MWNCT-Au/Pt with (a) MWCNT to Au/Pt volume ratio and (b) Pt concentration variations, with the inset image normalized to 475 nm to obtain better clarity in Au spectral changes at ~525 nm, (c) EDX mapping of the 3/100 nanocomposite, and (d) XPS spectrum of the 3/100 nanocomposite variation.

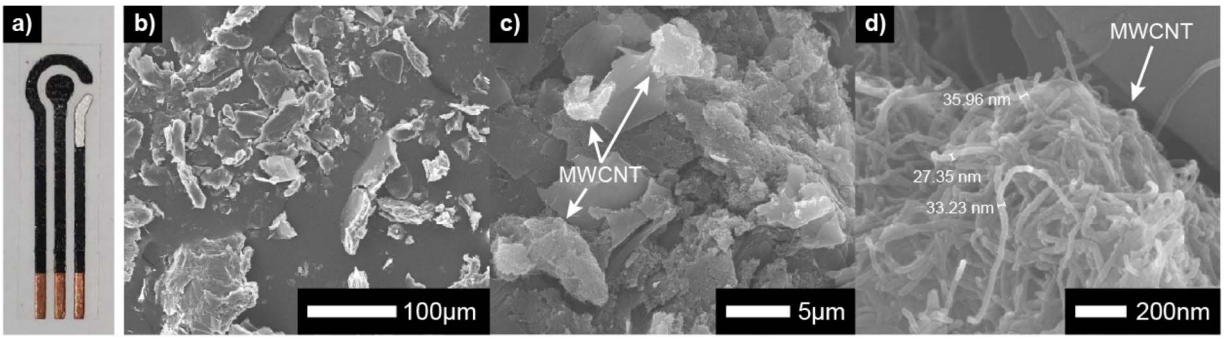

Fig. 4 (a) A photograph of fabricated SPE and (b–d) SEM images of the working electrode under different magnification.

with the role of PVP as a stabilizing and capping agent. These EDX results complement the UV-vis observations of controlled nanoparticle formation.

Further analysis to investigate the interatomic bonding within the nanocomposite is conducted using XPS, as shown in Fig. 3(d). The XPS spectra reveal a dominant presence of carbon (C 1s) and oxygen (O 1s) atoms, primarily originating from the MWCNT matrix, which contains active carboxylic acid (–COOH) functional groups. In contrast, Au (Au 4f) and Pt (Pt 4f) signals are detected at very low concentrations (~0.1%), likely due to the relatively small molar fraction of Au and Pt (~3% of the total molar content). Despite these limitations, the detection of Au and Pt albeit in small amounts supports the findings from previous characterizations, thereby confirming the successful formation of the MWCNT-Au/Pt nanocomposite.

Surface characteristic of fabricated SPE

The screen-printed electrode was successfully fabricated on a commercial-grade sticker paper as shown in Fig. 4(a). Subsequently, nanocomposite modification of the SPE was achieved using the drop-casting method. The fabricated SPE exhibits a relatively uniform thickness of 35.87 ± 1.57 μm, while the modified working electrode area reaches a thickness of 77.5 ± 5.59 μm. As shown in the SEM image in Fig. 4(b), carbon flakes from the carbon conductive paste are clearly visible with an average flake diameter of 28.36 ± 4.19 μm. At higher magnification in Fig. 4(c), clusters of MWCNTs are observed with an average diameter of 4.90 ± 1.33 μm. Further magnification in Fig. 4(d) reveals individual MWCNTs with diameters averaging 31.09 ± 6.94 nm, which aligns with the specified diameter range of 40 nm provided by the manufacturer. However, using SEM at this magnification level, the presence of Au and Pt nanoparticles could not be visually confirmed.

TEM image in Fig. 5(a) was acquired at a higher magnification with a 100 nm scale bar, where individual MWCNTs are observed in projection. The MWCNTs do not appear as continuous fibers but rather as globular or cluster-like features from carbon that are connected to form elongated structures. Such TEM observations are consistent with previously reported studies.[33] The present nanoparticles on the MWCNT are confirmed to be the Au and Pt with EDX as seen in Fig. 5(b), with the average diameter of 4.44 ± 0.66 nm and 4.26 ± 0.79 nm, respectively. Larger Au/Pt aggregates were also observed, with several clusters located outside the MWCNTs. This aggregation is likely caused by sonication process, during which elevated solution temperatures provided sufficient energy for nanoparticle growth and clustering. Gold nanoparticles exhibit a prism-like morphology as seen in Fig. 5(c), indicating distinct growth characteristics, and are observed to grow individually up to ~20 nm or aggregate into larger clusters of ~40 nm. Observing only the platinum nanoparticles as seen in Fig. 5(d), the nanoparticles maintain an average size of 4.81 ± 0.96 nm, consistent with the EDX mapping result.

The surface morphology of the SPE plays an important role in determining its wettability, and it is desirable that nanocomposite modification does not increase the SPE's hydrophobicity. As shown in the contact angle measurements in Fig. 6(a), a decreasing trend in contact angle is observed with lower

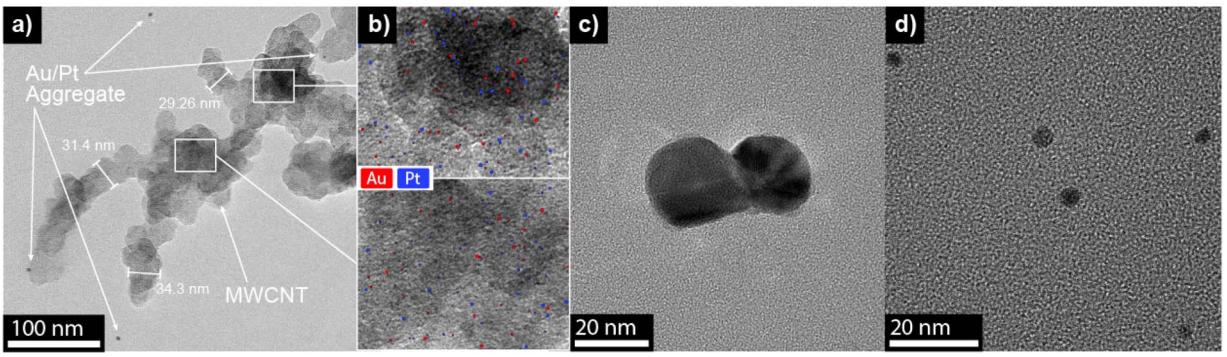

Fig. 5 TEM images of synthesized (a) MWCNT-Au/Pt with (b) the element analysis, and TEM of (c) Au aggregate and (d) Pt NPs.

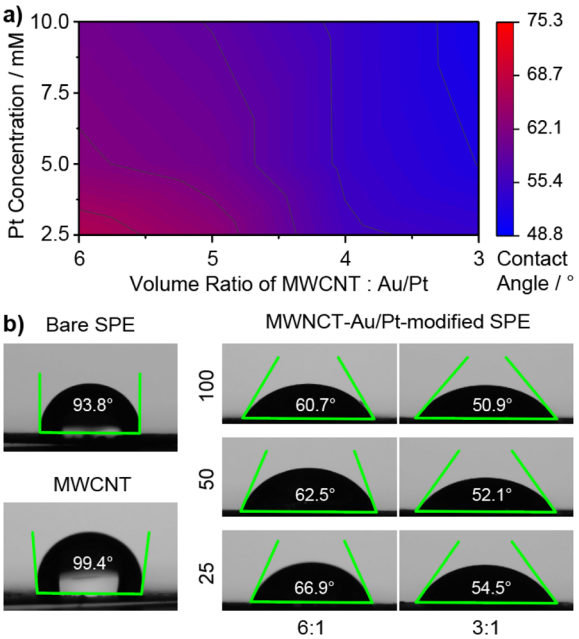

Fig. 6 (a) Hydrophobicity graph and (b) contact angle images of SPEs.

volume ratio of MWCNT to Au/Pt, indicating an increase in surface hydrophilicity. This trend can be attributed to the inherent hydrophobic nature of MWCNTs. Therefore, as the proportion of Au/Pt increases, a larger portion of the electrode surface is covered by Au and Pt rather than MWCNTs. Interestingly, even at the highest ratio of 6 : 1, the modified SPE remains more hydrophilic than the bare SPE, suggesting that the nanocomposite modification enhances the surface properties of the SPE. A similar pattern is observable with increasing Pt concentration. The increased Pt content may further improve hydrophilicity by filling the porous surface of the SPE.

The effects of nanoparticles on surface roughness of SPE is shown in Fig. 7(a), where a lower MWCNT-to-Au/Pt ratio led to a reduction in the average roughness of the SPE surface. Compared to bare SPE with the average roughness of 25.76 ± 1.64 μm, the modified SPE shows smoother surface. This effect is attributed to the filling of surface pores by the nanocomposites, thereby reducing surface roughness. Although the 4/25 variation appeared less porous compared to 6/25 and 5/25, the colour map revealed a greater presence of dark regions. Specifically, the 6/25 and 5/25 variations exhibited roughness deviations of 0.97 μm and 0.88 μm, respectively, while the 4/25 variation showed a higher standard deviation of 1.04 μm, indicating localized areas of increased roughness. This may be related to the agglomeration of the 4/25 variation, as supported by the relatively high absorption observed for the 4/25 variation in previous UV-vis characterization. In contrast, the 3/25 variation showed fewer dark regions, suggesting a more homogeneous surface morphology with a lower roughness deviation of 0.77 μm. Overall, the surface roughness results correlate with the contact angle measurements as seen in Fig. 7(b), both of which decreased as the ratio of MWCNT to Au/Pt reduced.

In addition to enhancing surface hydrophilicity, nanocomposite modification of the SPE also significantly improves its surface conductivity. Sheet resistance measurements revealed that the bare SPE exhibited relatively high resistance with considerable variability, *i.e.,* 29.75 ± 13.42 Ω/□. Incorporation of MWCNTs reduces both resistance and the deviation, yielding 22.55 ± 7.41 Ω/□. Further modification with MWCNT-Au/Pt nanocomposites results in a substantial decrease in resistance along with very low deviation down to 16.44 ± 0.77 Ω/□. As shown in Fig. 8, a clear trend of decreasing sheet resistance is observed as the volume ratio of MWCNT to Au/Pt decreased, reaching 9.84 ± 1.38 Ω/□. This highlights the role of Au and Pt nanoparticles in enhancing the electrical conductivity of the SPE surface. However, an increase in sheet resistance is observed with higher Pt concentrations. This may be attributed to residual PVP which forms a thin layer around the working electrode, therefore hindering electrical conductivity. To address this issue, more rigorous and repeated post-

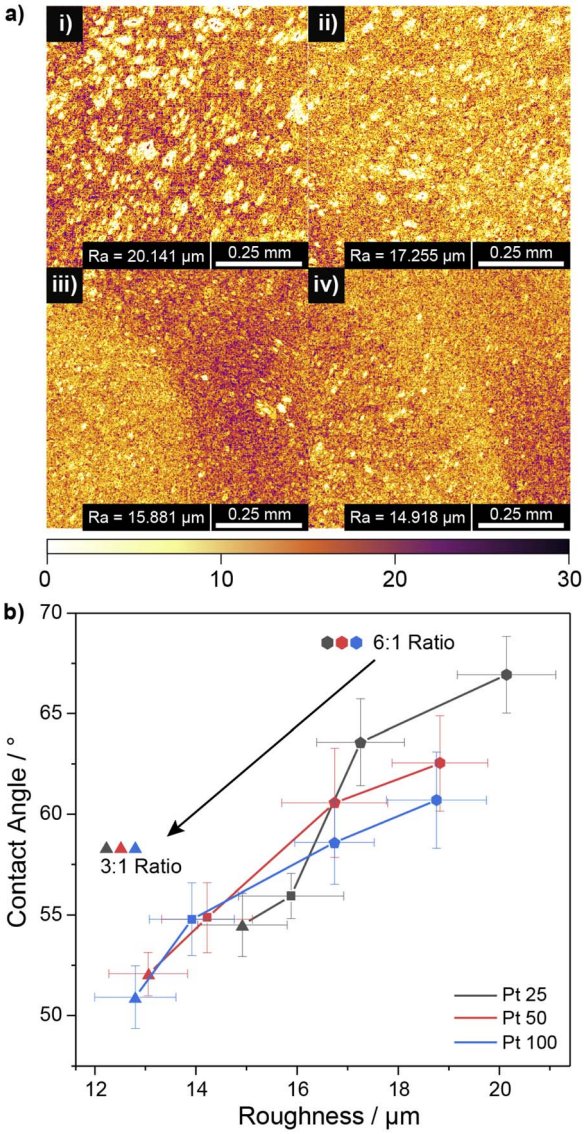

Fig. 7 (a) Surface roughness map of (i) 6/25, (ii) 5/25, (iii) 4/25, and (iv) 3/25 MWCNT-Au/Pt variations and (b) correlation of surface roughness with contact angle results.

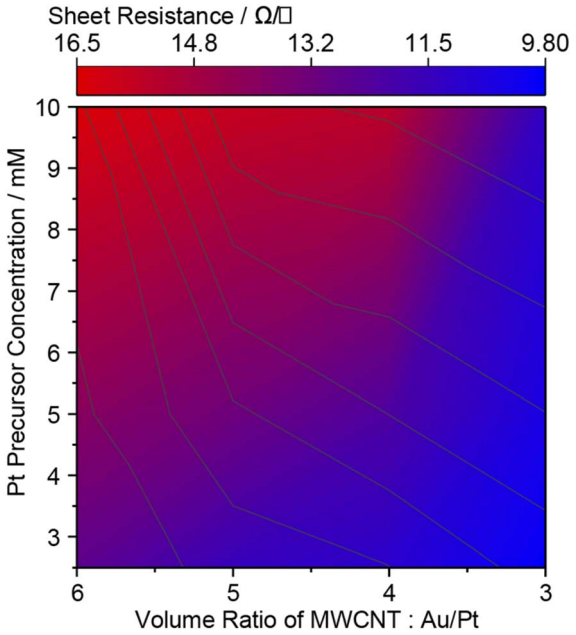

Fig. 8 Sheet resistance result of all SPE variations.

synthesis cleaning procedures are recommended to ensure thorough removal of PVP residues.

Electrochemical characteristic of fabricated SPE

Electrochemical characterization using cyclic voltammetry of 10 mM methylene blue solution with 1× PBS for SPEs modified with various MWCNT-Au/Pt ratios is presented in Fig. 9. The results show a clear trend in which bare SPEs exhibit lower peak currents compared to modified SPEs. Furthermore, as shown in Fig. 9(a), peak current increases with decreasing volume ratio of MWCNT to Au/Pt. This increase is attributed to the characteristic of each nanocomposite precursors, where MWCNTs increase the electroactive surface area, while Au and Pt nanoparticles enhance conductivity and serve as surface catalysts. In addition, increased Au/Pt nanoparticle concentrations also improve the hydrophilicity of SPE, and therefore helping the adsorption of methylene blue.

Another notable trend observed in Fig. 9(b) is the increase in current with increasing Pt concentration up to 5 mM. However, further increases in Pt concentration beyond this point lead to a decline in peak current. This decrease is in a good agreement with earlier conductivity results. Notably, at lower Pt concentrations, such as 5 mM, the catalytic effects of Pt as surface catalyst to adsorb the methylene blue overcome the low conductivity property, resulting in improved electrochemical performance. Previous results show that the best conductivity was obtained with lower Pt concentrations and lower MWCNT to Au/Pt ratios, whilst higher Pt concentrations combined with lower MWCNT to Au/Pt ratios provided the best hydrophilicity. CV measurements further indicate that lower ratios produced better results, with the 3 : 1 ratio determined as the most suitable for further use. As comparison, 5 mM of Pt is considered better alternative since it provided the best CV performance while maintaining acceptable conductivity and offering more consistent hydrophilicity compared to 2.5 mM of Pt. Therefore, the optimal variation is determined to be a 3 : 1 volume ratio with a Pt concentration of 5 mM which later being used for subsequent testing of secondary metabolites.

Electrochemical impedance spectroscopy (EIS) was performed to evaluate both the bare SPE and the MWCNT-Au/Pt-modified SPE as seen in Fig. 10. The Nyquist plot shows two semicircles which corresponded to the charge transfer reaction at high and medium frequency. The impedance data, *i.e.* Nyquist plot is fitted using an equivalent circuit model consisting of three resistors, where R_2 and R_3 are each connected in parallel with a constant phase element (CPE), as illustrated in Fig. 10(c). In this model, R_1 represents the resistance of the electrochemical cell. The R_2Q_2 represents the charge transfer at the counter electrode occurring at high frequency, while the R_3Q_3 represents the charge transfer reaction at working electrode interface. The exponent n in the CPE reflects the surface characteristics of the electrode with n approaching 1 suggest a smooth surface, while $n \sim 0.5$ indicates a more porous surface.[25] Compared to bare SPE, the results show that the n increased with nanocomposite modification. This trend is consistent with the surface roughness, where the n rose from 0.93 to 0.96 as the surface became more homogeneous with decreasing MWCNT ratios.

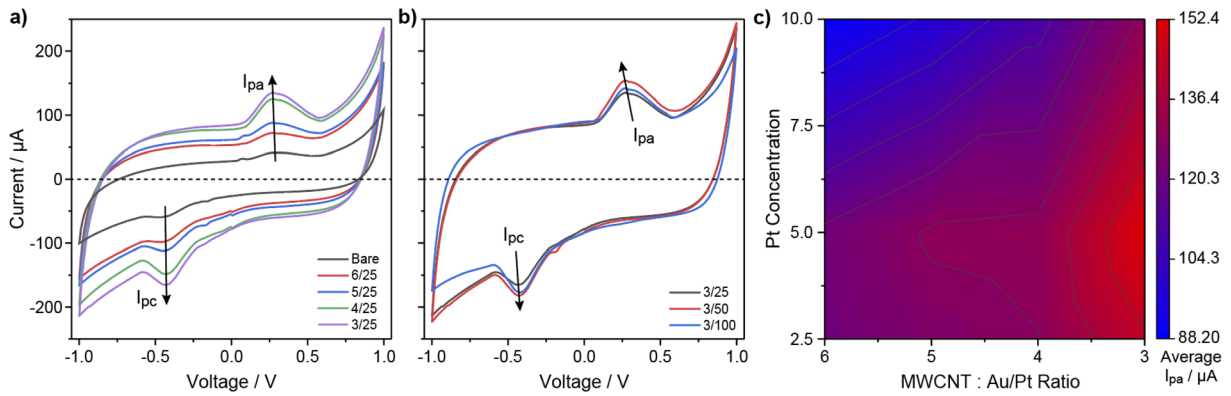

Fig. 9 CV result of (a) bare and modified SPEs with different ratios, (b) modified SPEs with different Pt concentrations, and (c) summarized result.

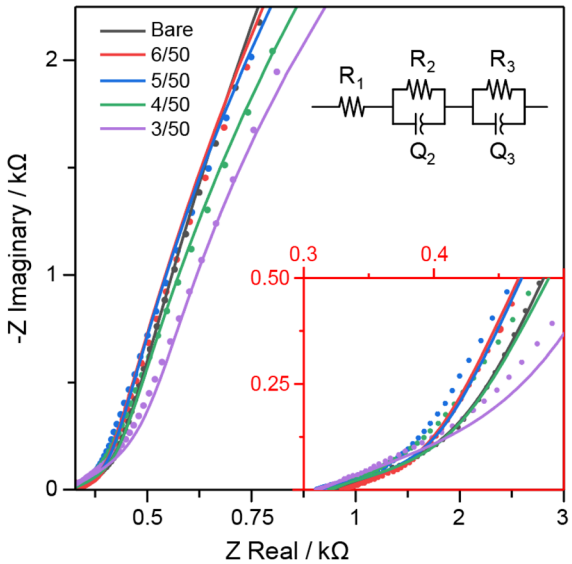

Fig. 10 Nyquist plot of impedance analysis result of bare and modified SPE along with the equivalent circuit model.

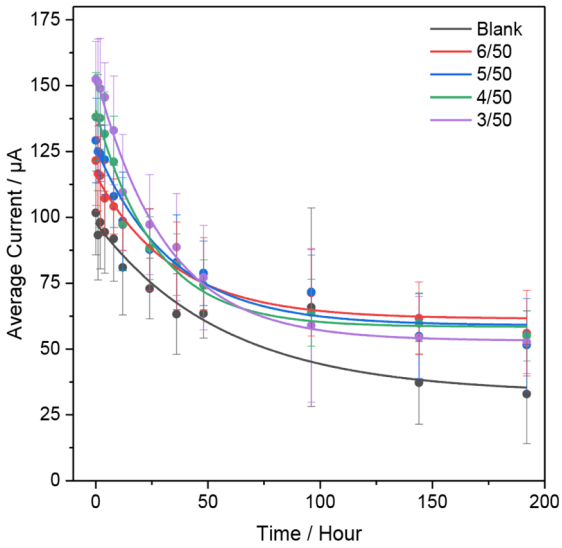

Fig. 11 Current result of periodic CV measurement of continuously immersed SPEs.

The fitted impedance parameters are summarized in Table 1, showing good-fit results with errors below 10%. The R_1 and R_2 show slight difference across the different SPE variations, likely due to the carbon paste conductivity, as previously observed in the four-point probe measurements. Notably, the incorporation of MWCNT-Au/Pt nanocomposites lead to a significant reduction in R_3, indicating improved charge transfer at the working electrode. Among the SPE variations, the volume ratio of 3 : 1 shows the lowest R_3, consistent with the earlier CV results. This reduction in resistance suggests an enhancement in the electroactive surface area and surface conductivity, primarily attributed to the conductive properties of Au and Pt.

The stability test of the SPE, conducted through continuous immersion in electrolyte with periodic CV measurements, is presented in Fig. 11. Both the modified and bare SPEs maintain relatively stable anodic peak current during the initial 2 hour period. No significant current fluctuations are observed, with the average current variation across five different SPEs for both bare and modified SPEs remaining below 10 μA. However, a gradual increase in standard deviation is noted over time, indicating growing variability among the samples during prolonged immersion. At extended immersion durations, notable degradation is observed. The calculated time constants show significant performance drops at approximately 57.1 hours for the bare SPE and 34.5 hours for the 6/50 variation of MWCNT-Au/Pt-modified SPE. Lower MWCNT ratios further reduces stability, with time constants of 33.49 hours for the 5/50 variation and 30.91 hours for the 3/50 variation. The 4/50 variation shows the shortest time constant of 26.49 hours, likely due to notable nanocomposite agglomeration as indicated in previous discussion, which may weaken adhesion to the electrode surface. At these degradation points, the recorded currents decrease to less than 50% of their initial current. Overall, the results suggest that SPEs exhibit stable performance within the first 2 hours of operation, allowing limited reuse within this timeframe. However, the reduced long-term stability highlights their suitability as single-use, disposable sensing devices, consistent with their intended design.

Secondary metabolites detection

The detection result of secondary metabolites was obtained through DPV current as seen in Fig. 12. The DPV results show a decreasing current trend with increasing phytol concentration from 5 μM to 50 mM. This decline is attributed to the adsorption of phytol onto the surface of the SPE. Phytol, a chlorophyll-derived diterpene alcohol, is highly hydrophobic and nonpolar due to its long carbon chain.[43,44] As non-electroactive analyte, phytol does not actively participate in electron transfer but instead adsorbs onto the similarly hydrophobic carbon surface of the electrode. This interaction, primarily driven by van der Waals forces, leads to surface blocking, which hinders electron

Table 1 Fitting parameter of EIS

SPE	R_1 (Ω)	R_2 (Ω)	Q_2 (μF s^{1-N})	n_2	R_3 (kΩ)	Q_3 (μF s^{1-N})	n_3	Error (%)
Bare	327	126.7	0.67	0.55	61.59	0.28	0.83	3.09
6/50	319	115.2	0.10	0.56	45.46	0.36	0.93	4.81
5/50	313	131.1	0.10	0.58	41.79	0.39	0.94	9.43
4/50	318	122.4	0.12	0.54	28.54	0.36	0.96	6.75
3/50	309	137.1	0.11	0.58	19.44	0.37	0.96	9.92

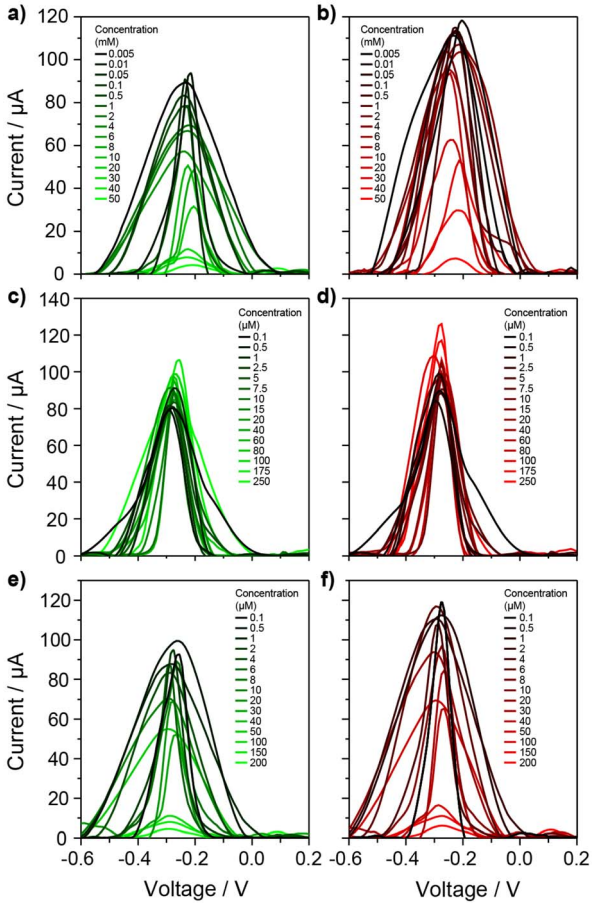

Fig. 12 DPV current of bare SPE (left) and 3/50-modified SPE (right) for detection of (a and b) phytol, (c and d) quinoline, and (e and f) stigmasterol.

transfer between the electrode and the PBS electrolyte, resulting in a reduced electrochemical current.[28,45]

A contrasting pattern is observed in the detection of secondary metabolite quinoline, as shown in Fig. 12(c and d). The results demonstrate an increasing current response with rising quinoline concentrations from 100 nM to 250 μM. Unlike phytol, quinoline (2,3-benzopyridine) is electroactive and undergoes electrooxidation to form quinolinic acid (pyridine-2,3-dicarboxylic acid), which contributes to the increase in current.[22]

The detection of different secondary metabolite stigmasterol showed a current response similar to that of phytol. As shown in Fig. 12(e and f), increasing stigmasterol concentrations from 100 nM to 200 μM results in a gradual decrease in current. In plant metabolism, stigmasterol acts as a transport inhibitor, affecting the movement of ions and hormones within cells.[46] Similar to phytol, stigmasterol is also a nonpolar and non-electroactive compound. Stigmasterol can also adsorb onto the hydrophobic carbon surface of the electrode, forming weak interactions that block active sites and hinder electron transfer, therefore decreasing the current.[28]

Linear regression is applied to the DPV peak currents for the detection of each compound, with the resulting calibration curves presented in Fig. 13 and the corresponding regression parameters summarized in Table 2. For phytol detection, the fitting results indicate good model fits, with R^2 exceeding 0.95. Compared to bare SPEs, the modified SPE exhibits better performance across all parameters. The best result is obtained with an R^2 of 0.98 and a LOD of 2.85 mM.

For quinoline detection, the fitting shows good linearity, although the bare SPE showed much lower linearity compared to the modified SPE. Consistent with earlier findings, the MWCNT-Au/Pt-modified SPEs exhibits better performance, achieving the best result with an R^2 of 0.95 and an LOD of 2.36 μM. Although previous study has reported quinoline detection down to the nanomolar range, those approaches often employed electrodeposition techniques with multilayer coatings to achieve highly uniform and optimized surfaces.[22,47] While such methods yield higher sensitivity, they are less suitable for scalable, low-cost fabrication. Additionally, the detection utilized commercial SPEs, whereas the SPEs in this study were manually fabricated and modified using a drop-casting method. Therefore, achieving an LOD in the low micromolar range remains a commendable result and demonstrates the viability of the approach used in this work.

For stigmasterol detection, although the compound was tested over a concentration range of 0.1–200 μM, regression is only performed over the linear range of 0.1–100 μM to obtain the highest linearity. The results also demonstrate good model fits, with R^2 exceeding 0.95 for both bare and modified SPE. As

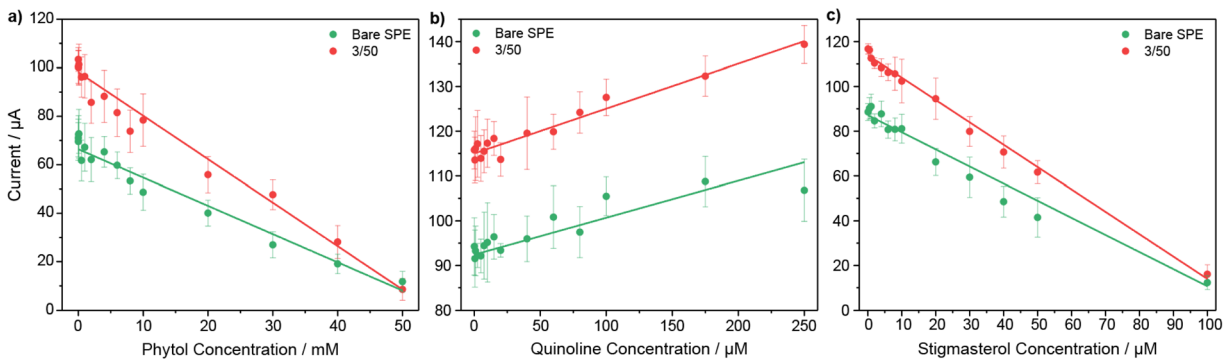

Fig. 13 Calibration curve of DPV current for the detection of (a) phytol, (b) quinoline, and (c) stigmasterol.

Table 2 Calibration curve parameter of secondary metabolites detection using DPV

	Phytol		Quinoline		Stigmasterol	
Parameter	Bare	Modified	Bare	Modified	Bare	Modified
R^2	0.970	0.984	0.901	0.945	0.968	0.976
Sensitivity	-1.166 μA mM^{-1}	-1.794 μA mM^{-1}	0.083 μA μM^{-1}	0.100 μA μM^{-1}	-0.765 μA μM^{-1}	-1.000 μA μM^{-1}
RSD (%)	13.84	9.88	5.65	4.26	14.38	9.63
LOD	4.85 mM	2.85 mM	16.63 μM	2.36 μM	4.86 μM	1.36 μM
LOQ	17.73 mM	8.64 mM	50.39 μM	7.15 μM	14.72 μM	4.12 μM

with the previous detections, the modified SPEs consistently exhibit better performance in all parameters. The best result is obtained with an R^2 of 0.98 and an LOD of 1.36 μM. This performance slightly surpasses that reported in a previous study, which achieved an LOD of 1.5 μM using commercial SPEs.[28] Although the linearity achieved in this study is marginally lower than previous study, the use of accessible, low-cost, manually fabricated SPEs highlights the potential of this method as an effective alternative for electrochemical detection of secondary metabolites, offering comparable sensitivity to that of commercial platforms.

In addition to DPV measurements, chronoamperometry is conducted for comparative analysis, with the results presented in Fig. 14(a–c). The current response trends observed are consistent with those obtained from DPV, *i.e.* a decrease in current with increasing concentrations of phytol and stigmasterol and an increase in current with rising quinoline concentrations. Exponential fitting is used to determine the time constant as the average current decay times for each compound. For phytol detection, the bare SPE exhibits a time constant of 18.26 ± 2.3 seconds, while the MWCNT-Au/Pt-modified SPE reached a stable current more quickly, with time constant of 17.44 ± 2.2 seconds. In the case of quinoline, the bare SPE is characterized by a time constant of 19.01 ± 3.2 seconds, whereas the modified SPE shows improved response speed with a time constant of 15.72 ± 2.5 seconds. Similarly, for stigmasterol detection, the time constant for the bare SPE is 19.43 ± 2.5 seconds, compared to 17.44 ± 2.9 seconds for the MWCNT-Au/Pt-modified SPE. These results suggest that nanocomposite modification not only enhances sensitivity but also improves the electrode's response time, supporting its effectiveness in electrochemical sensing applications.

Linear regression is performed on the lowest current obtained from chronoamperometry, with the resulting calibration curves presented in Fig. 14(d–f) and the corresponding regression parameters are summarized in Table 3. For phytol detection, the results are consistent with those obtained from DPV, showing strong linearity with $R^2 > 0.95$ across all SPE types. Similar with the DPV analysis, the detection using chronoamperometry with MWCNT-Au/Pt-modified SPEs

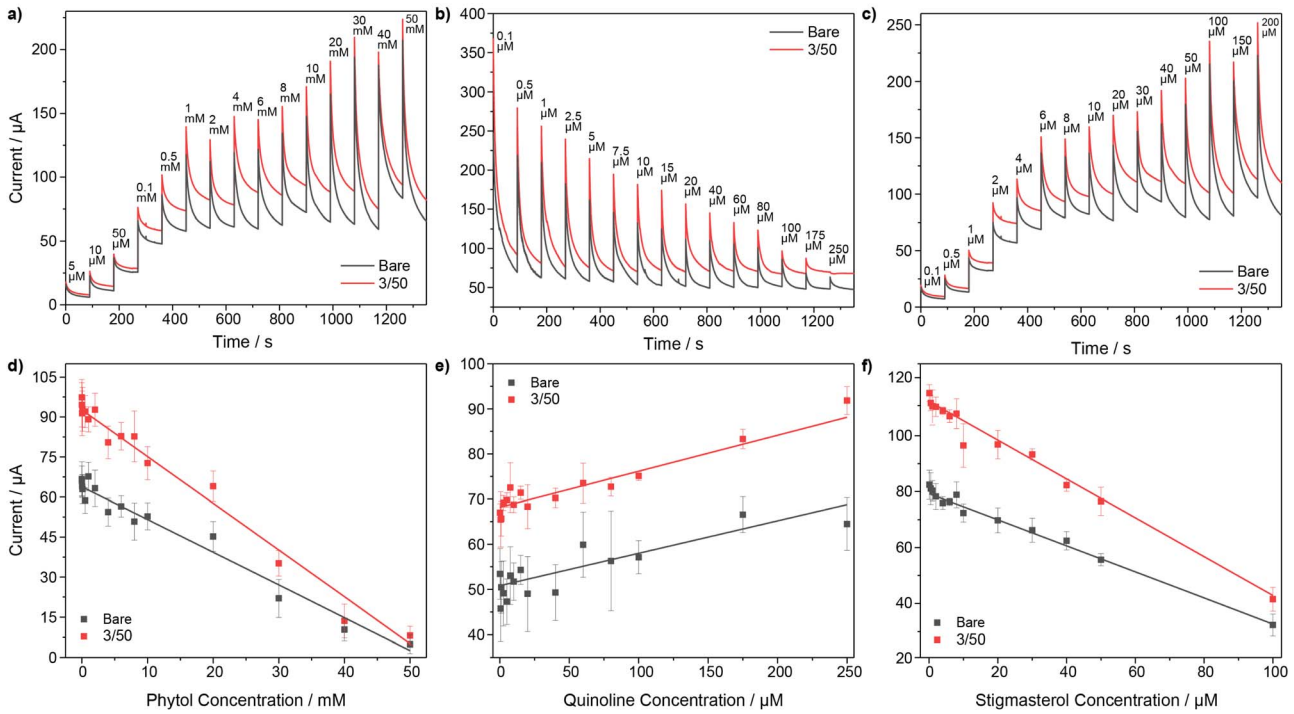

Fig. 14 Chronoamperometry results (top) and calibration curve results (bottom) for the detection of (a and d) phytol, (b and e) quinoline, and (c and f) stigmasterol.

Table 3 Calibration curve parameter of secondary metabolites detection using chronoamperometry

	Phytol		Quinoline		Stigmasterol	
Parameter	Bare	Modified	Bare	Modified	Bare	Modified
R^2	0.955	0.958	0.859	0.908	0.972	0.973
Sensitivity	-1.230 μA mM^{-1}	-1.750 μA mM^{-1}	0.072 μA μM^{-1}	0.080 μA μM^{-1}	-0.462 μA μM^{-1}	-0.688 μA μM^{-1}
RSD (%)	14.05	9.74	11.42	4.07	9.17	7.04
LOD	4.91 mM	3.03 mM	15.30 μM	3.98 μM	4.85 μM	2.32 μM
LOQ	14.88 mM	9.18 mM	46.36 μM	12.06 μM	14.70 μM	7.03 μM

demonstrate superior performance, achieving the best result with an R^2 of 0.96 and a limit of detection (LOD) of 3.02 mM. Quinoline detection follows a similar trend, though with slightly lower performance compared to DPV. The bare SPE exhibited a notably lower R^2 of 0.86, while the MWCNT-Au/Pt-modified SPEs again showed better performance, achieving an R^2 of 0.91 and an LOD of 3.98 μM. For stigmasterol, chronoamperometry results also aligned with DPV findings. The regression models displayed good fits, with $R^2 > 0.95$ for both electrode types. The modified SPEs maintain their advantage, delivering the best performance with an R^2 of 0.97 and an LOD of 2.32 μM.

The average RSD across the concentration ranges used for calibration shows the improvement of measurement precision with the modification of SPE for both DPV and chronoamperometric techniques. In DPV measurement, the modified SPE exhibits lower RSDs for phytol (9.88% *vs.* 13.84%) and stigmasterol (9.63% *vs.* 14.38%) compared to the unmodified SPE, indicating enhanced stability, while quinoline shows consistently low RSD for both electrodes, with a slight improvement after modification (4.26% *vs.* 5.65%). A similar trend is observed for chronoamperometry, where the modified SPE yields lower average RSDs for all analytes, particularly for quinoline (4.07% *vs.* 11.42%) and stigmasterol (7.04% *vs.* 9.17%). These results align with the previous result that the modification of SPE improves the repeatability and reduces measurement variability.

The comparison between DPV and CA can be seen in Fig. 15. Overall, the DPV method exhibited better performance compared to chronoamperometry. This advantage stems from DPV's ability to scan a broad potential range (−0.8 V to 0.6 V) and suppress capacitive current through pulsed measurements, thereby enhancing signal clarity and producing more distinct peaks.[48] However, DPV analysis typically requires additional data processing, such as baseline subtraction. In contrast, chronoamperometry offers a more straightforward, direct output without post-processing, making it more practical for rapid screening. Furthermore, the time constants for current stabilization across all three analytes were under 20 seconds, reinforcing chronoamperometry's suitability for rapid detection applications. While DPV offers greater analytical sensitivity, chronoamperometry presents an alternative method for rapid, low-complexity measurements. The performance of the fabricated SPEs is comparable to that reported in previous studies on the detection of *Ganoderma*-related secondary metabolites. In certain cases, the results even surpass those of earlier works, despite the use of manually fabricated SPEs and a simple drop-

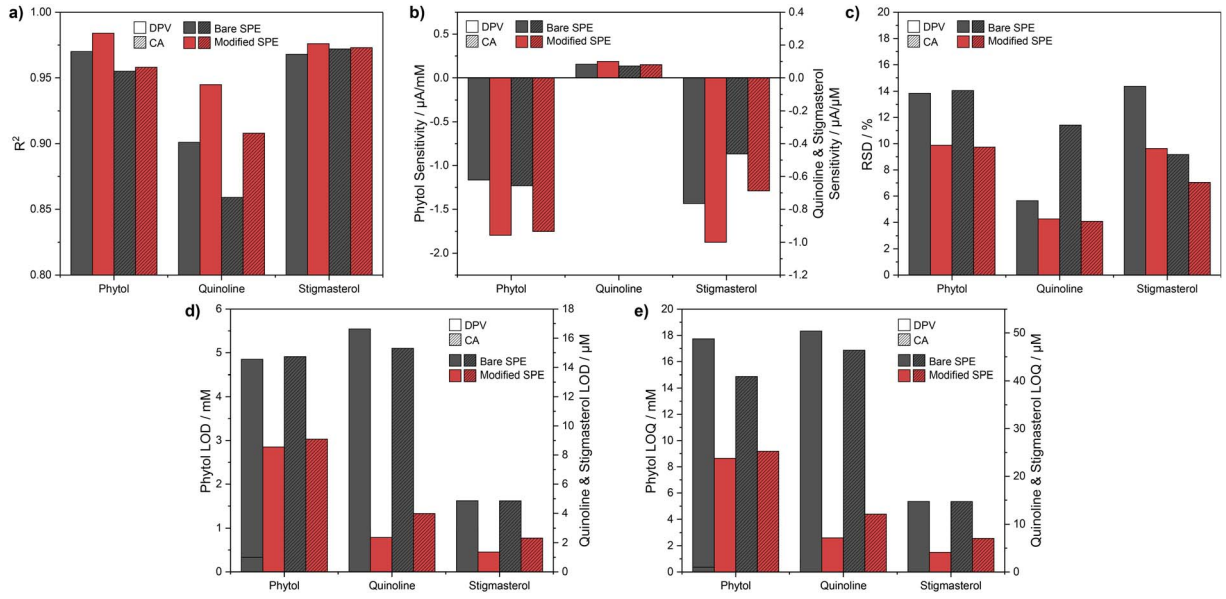

Fig. 15 Summary of sensing parameters of (a) R^2, (b) sensitivity, (c) RSD, (d) LOD, and (e) LOQ using DPV and CA for all metabolites.

Table 4 Comparison of detection performance with previous studies in *Ganoderma*-related detection using SPE

Analyte	Electrode material	Method	Range	LOD	Ref.
Quinoline	AuNPs-aMWCNTs/CTSNPsaMWCNTs	CV, LSV	0.0004–1.0 μM	3.75 nM	39
Palmitic acid	rGO/AuNPs	LSV	0.1–0.83 mM	0.015 mM	41
Crude leaf extract	ZnO-NPs/rGO	DPV	10–40 mg L^{-1}	1.75 mg L^{-1}	13
Stigmasterol	β-CD-rGO/AuNPs	DPV	2–30 μM	1.5 μM	25
Phytol	MWCNT-Au/Pt	DPV	0.005–50 mM	2.85 mM	This work
Phytol		CA		3.03 mM	
Quinoline		DPV	0.1–250 μM	2.36 μM	
Quinoline		CA		3.98 μM	
Stigmasterol		DPV	0.1–250 μM	1.36 μM	
Stigmasterol		CA		2.32 μM	

casting method for modification in this study. A summary of the performance comparison is presented in Table 4.

Evaluation of multi-analyte detection

The sensor selectivity was obtained through PCA analysis with the result as shown in Fig. 16(a). The result showed that PC1 is the dominant discrimination axis, representing the direction of maximum variance or the largest data spread, accounting for 68.8% of the total variance. PC2 represents the secondary modulation or the next most significant direction, contributing 31.2% of the variance. In the PCA score plot, phytol and quinoline appear more distinctive compared to stigmasterol. Stigmasterol is distributed near the center with a broad spread and overlaps with the regions occupied by phytol and quinoline. Phytol is located mostly in the negative PC1 region, whereas quinoline is strongly positioned in the positive PC1 region, which makes these two metabolites highly distinctive from each other. Overall, the PCA plot still demonstrates clear separation among the metabolites along PC1.

The PCA loading (weighting) shows that the current contributes a positive value of 0.707107 to PC1, while the voltage contributes negatively of −0.707107 to PC1. When correlated with the PCA score plot, this indicates that phytol exhibits relatively low current with higher potential behavior, quinoline shows relatively higher current with lower potential behavior, and stigmasterol displays intermediate electrochemical behavior without a distinct characteristic trend. For PC2, both current and voltage contribute positively of 0.707107, indicating that PC2 represents the overall electrochemical response intensity.

Subsequently, the result of LDA analysis for the sensor specificity was obtained as shown in Fig. 16(b). The histogram represents LD1, which is the linear combination of current responses across voltage that maximizes between-class separation relative to within-class variance. LD1 captures the dominant electrochemical differences among phytol, quinoline, and stigmasterol, where separation along LD1 reflects differences in peak shape, peak intensity distribution, and/or peak position, rather than merely voltage location.

Quinoline is strongly clustered in the LD1 range of approximately −2.5 to −1, showing a narrow distribution that indicates high specificity of quinoline detection and low intra-class variance, with minimal overlap with other classes. Stigmasterol is broadly distributed between approximately LD1 −1.5 to 3 and partially overlaps with phytol at positive LD1. The low frequency across LD1 indicates that stigmasterol is less distinct for classification. Phytol is less distinctive than quinoline and is mainly distributed between LD1 of approximately 1 to 3, overlapping with stigmasterol in the LD1 range of about 0.5 to 2.5. Overall, the specificity is good but not absolute, particularly with respect to stigmasterol.

The LDA classification accuracy is 0.83, while the five-fold random cross-validation accuracy is 0.74. Fig. 16(c) shows the normalized confusion matrix obtained from the LDA computation. This matrix clearly demonstrates the specificity of phytol and quinoline, as both were classified with 100% correctness, indicating that they are electrochemically distinctive. In contrast, stigmasterol shows lower specificity, with only 35% correctly classified, while 30% are misclassified as phytol and 35% as quinoline, suggesting that stigmasterol shares partial electrochemical features with the other two metabolites.

The interference study assessed the quantitative accuracy of phytol, quinoline, and stigmasterol determination in binary mixtures by comparing the measured concentration in the mixture to the concentration of the individual metabolite, with the results shown in Fig. 16(d). Low interference values (<10%) were observed when each target metabolite was quantified in the presence of palmitic and linoleic acids. Phytol exhibited moderate interference in the presence of quinoline (∼15%), and similarly, quinoline showed moderate interference when combined with phytol (∼17%). In contrast, both phytol and quinoline showed strong interference when combined with stigmasterol (>20%), suggesting partial overlap in electrochemical response, which aligns with the previous analysis.

The high interference can be attributed to the similar electrochemical detection mechanisms of these metabolites on the SPE surface. When two metabolites are present simultaneously, shifts in peak potential toward closer values were observed, often resulting in partial or complete peak overlap. This peak convergence leads to a single broadened or merged DPV signal, which affects peak assignment and causes deviations in the measured concentrations. In contrast, the addition of linoleic acid or palmitic acid does not significantly affect either the peak potential or peak current of quinoline, phytol, or stigmasterol. The electrochemical responses of these fatty acids occur outside the potential window of the target metabolites,

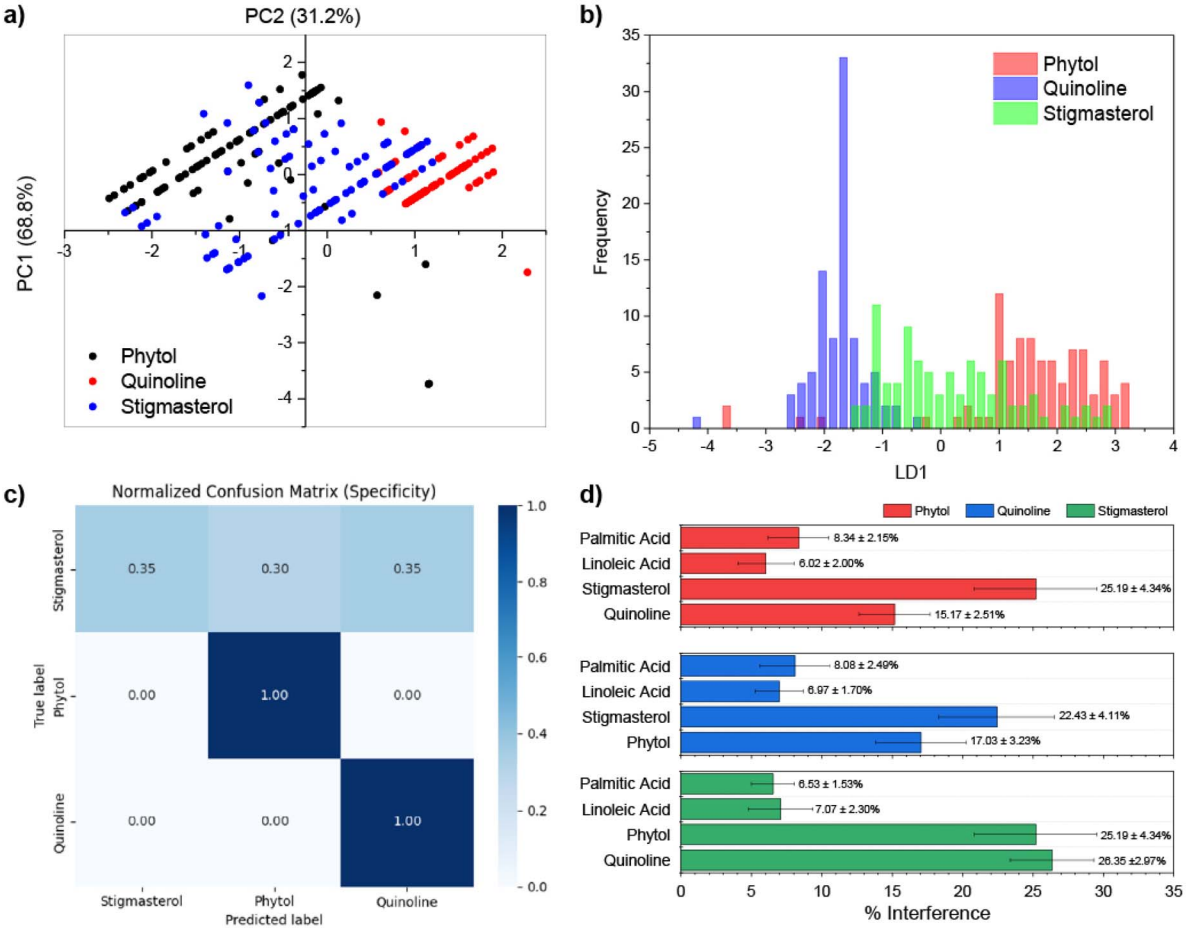

Fig. 16 (a) Scatter plot of PCA, (b) histogram of LDA result with (c) the normalized confusion matrix obtained from the LDA computation, and (d) interference test of binary mixture of metabolites.

minimizing electrochemical cross-talk and resulting in negligible interference.

Furthermore, the direction of current change differs among the target metabolites. Increasing quinoline concentration increases the current response, whereas phytol and stigmasterol reduce the current. Consequently, when quinoline is present with phytol or stigmasterol, the obtained concentration of phytol or stigmasterol is lower than expected. Similarly, the mutual current suppression between phytol and stigmasterol further increases quantification errors when both metabolites coexist.

Detection of oil palm leaves extract

Additional evaluation of SPE performance was conducted using real samples of healthy and infected oil palm leaf extracts. The recovery study results are shown in Table 5. Overall, the method demonstrates good repeatability, with RSD ranging from 4.16% to 8.35%. Recoveries of phytol in healthy samples are found higher than 100%. This overestimation is likely due to overlapping contributions of quinoline and stigmasterol, similar with the interference test. In contrast, phytol recoveries in infected samples decreases to 87.63% and 79.23%. This reduction is presumably due to higher interference of other metabolites, *e.g.*, stigmasterol which present at higher concentrations in infected samples and contributes to current suppression. In addition, the comparison between spiked and measured concentrations shows that phytol levels in healthy leaves are substantially higher than the spiked values, with differences of more than 10 mM.

A previous study reported phytol levels of 29.21% in healthy seedlings and 14.10% in infected seedlings at 30 days old. Considering the extract concentration used in this work, these levels correspond to approximately 9.85 mM phytol for healthy leaves and 4.75 mM phytol for infected leaves. Therefore, phytol concentrations above 9.85 mM may indicate a healthy oil palm, whereas concentrations below 4.75 mM may suggest infection. The higher concentration observed in unspiked sample as seen in Fig. 17(b) may be attributed to the older plant age or interference. Infected leaves, by contrast, exhibits much lower phytol concentrations. This significant reduction is likely attributed to the severity of infection in the affected tree, which exhibited visible basidiocarp formation of *Ganoderma* as seen in Fig. 17(a), indicating advanced disease progression that has already affected and necrotized the leaves.[14] This finding is consistent with diseased conditions in previous work.[13]

Table 5 Detection of secondary metabolites in palm leaf extracts

Biomarker	Sample	Added conc.	Found conc.[a]	RSD[a] (%)	Recovery[a] (%)
Phytol	Healthy	20 mM	32.72 mM	6.63	111.01
		6 mM	17.97 mM	7.01	125.11
	Infected	20 mM	21.10 mM	4.58	87.63
		6 mM	8.35 mM	8.02	79.23
Quinoline	Healthy	80 μM	67.86 μM	6.10	96.41
		20 μM	7.48 μM	6.70	89.10
	Infected	80 μM	76.94 μM	8.35	97.77
		20 μM	20.28 μM	6.79	109.63
Stigmasterol	Healthy	50 μM	71.77 μM	6.53	121.42
		20 μM	39.67 μM	9.79	124.90
	Infected	50 μM	96.93 μM	4.50	127.73
		20 μM	62.35 μM	5.82	131.95

[a] Found concentration, RSD, and recovery are obtained from the average of 6 replicates.

Stigmasterol shows low accuracy in healthy matrices, with recoveries of around 120%, indicating high matrix interference that causes discrepancies between the added and recovered concentrations. Higher recoveries (127–131%) are observed in infected samples, suggesting even greater interference from other metabolites besides phytol present in the leaf extracts. Nevertheless, the precision of stigmasterol measurements remains satisfactory, with RSD values lower than 10%, confirming good method reproducibility. In addition, a similar trend is observed for stigmasterol, with healthy leaf extracts showing a difference of more than 15 μM compared to the spiked concentration. By comparison, the reported stigmasterol concentration in infected oil palm trees is 5.37 μM in 3.5 month-old plants.[28] While the much higher concentration observed in this study can be attributed in part to interference effects, it may also reflect the severity of infection, similar to the trend observed for phytol. As shown in Fig. 17(b), infected leaves exhibit higher stigmasterol concentrations than healthy leaves, consistent with previous findings.

Quinoline exhibits the most consistent performance among the three biomarkers studied here. The recovery in both healthy (89.10–96.41%) and infected (97.77–109.63%) matrices are close to the ideal condition of 100%, demonstrating minimal matrix interference. This aligns with previous LDA result which shows that quinoline has narrow and high frequency of LD1 feature. The consistently low RSD (6.10–8.35%) further supports the high stability of quinoline detection. However, the measured concentrations in both healthy and infected extracts are consistently lower than the spiked amounts, resulting in negative unspiked concentrations, as shown in Fig. 17(b). This underestimation may be attributed to the presence of other interfering metabolites that reduce the overall current response, consistent with the interference study, which shows stable but lower quinoline signals. Nevertheless, infected leaves exhibit slightly elevated quinoline levels compared to healthy leaves, in good agreement with earlier reports.[12,47]

Overall, the fabricated SPEs exhibited limited selectivity. Selectivity could be improved by incorporating modifiers such as β-cyclodextrin, which forms host–guest inclusion complexes with stigmasterol.[28] The sensing is based on a competitive binding mechanism, where the analyte and an electroactive indicator compete for the same binding sites within the host cavity during electrochemical measurement. Upon addition of the target analyte to a solution containing host–indicator complex, the analyte displaces the indicator from the binding site, leading to a measurable change in the electrochemical signal. Cyclodextrins are cyclic oligosaccharides characterized by a hydrophobic inner cavity and a hydrophilic outer surface,

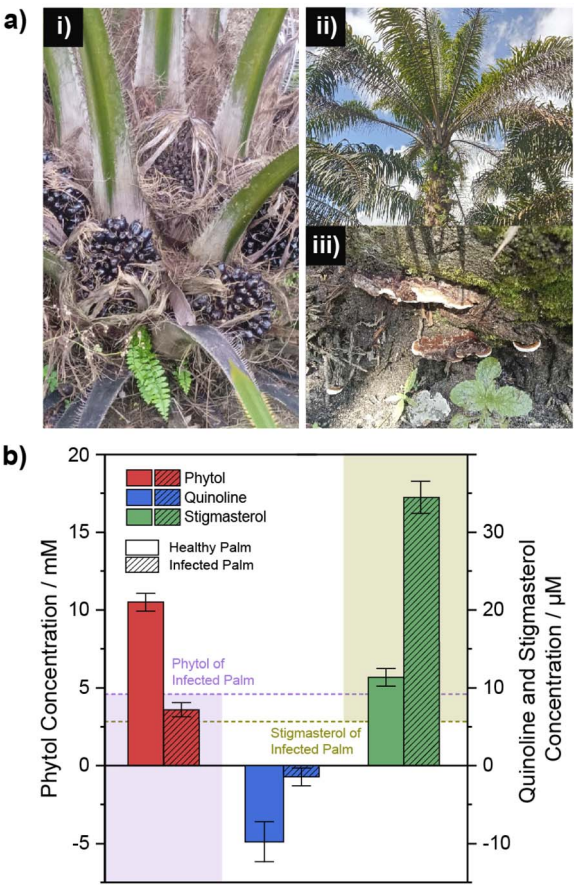

Fig. 17 (a) Real sample test of: (i) healthy and (ii) infected palm tree with (iii) *Ganoderma boninense* and (b) summary of secondary metabolites detection in palm leaf extracts.

enabling selective encapsulation of hydrophobic guest molecules. By exploiting these host–guest interactions, β-cyclodextrin-modified SPEs could enhance molecular recognition and reduce cross-interference, thereby improving selectivity toward stigmasterol and related hydrophobic metabolites in complex matrices. Despite these challenges, the lower LOD relative to metabolite levels in both healthy and infected leaves highlight the potential of SPEs for detecting secondary metabolites, especially phytol and stigmasterol.

Conclusions

This study successfully demonstrated the fabrication and modification of screen-printed electrodes using multi-walled carbon nanotubes combined with Au and Pt nanoparticles for the electrochemical detection of secondary metabolites associated with *Ganoderma boninense* infection. The simple and cost-effective fabrication and modification processes offer an alternative method for potential large-scale production. Two electrochemical detection methods were evaluated, each offering distinct advantages. The modified electrodes showed improved detection performance compared to bare SPEs, comparable, or some even exceeding, that of commercial SPEs reported in previous studies. The modified SPEs showed good linearity ($R^2 > 0.9$) across all detections, with the best detection limits achieved being 2.85 mM for phytol, 2.36 μM for quinoline, and 1.36 μM for stigmasterol.

Evaluation with real oil palm leaf extracts further validated the applicability of the developed SPEs. Phytol and stigmasterol were successfully detected, with concentrations in healthy and infected leaves reflecting expected physiological differences. Quinoline detection, however, remained unreliable due to interference effects, underscoring the current limitation in selectivity. While establishing a definitive metabolite profile for *G. boninense* infection may require analysis of additional biomarkers, the metabolites investigated in this study demonstrate potential as early indicators of abnormal physiological responses. The low LOD relative to metabolite concentrations in the leaves highlight the potential of the modified SPEs for practical secondary metabolite detection, particularly phytol and stigmasterol. Overall, the MWCNT-Au/Pt-modified SPE presents a promising alternative for the practical, rapid, and cost-effective detection of *G. boninense*-related biomarkers. These findings support its further development as a disposable biosensor for early disease diagnosis in oil palm plantation.

Author contributions

Arda F. Putra performed conceptualization, methodology, resources collection, data curation, investigation, formal analysis, visualization, and writing the original draft. Fadlilatul Taufany performed funding acquisition and reviewing the manuscript. Rio Akbar Yuwono performed resource collection, data curation, formal analysis, and reviewing of the manuscript. Chusnul Khotimah performed data curation, investigation, and reviewing of the manuscript. Fu-Ming Wang performed characterization and investigation, formal analysis, and reviewing of the manuscript. Chi-Hsien Huang performed investigation, formal analysis, and reviewing of the manuscript. Ruri A. Wahyuono performed conceptualization, supervision, funding acquisition, and reviewing and editing of the final draft.

Conflicts of interest

There are no conflicts to declare.

Data availability

The data supporting this article have been included as part of the supplementary information (SI). Supplementary information: experimental data, UV-vis and FT-IR spectra, XPS spectra, EDX, SEM and TEM images, contact angle and roughness test data, sheet resistance test, CV, EIS, DPV, and chronoamperometry data. See DOI: https://doi.org/10.1039/d5ra09886f.

Acknowledgements

The author expresses sincere gratitude to Institut Teknologi Sepuluh Nopember (ITS) and National Taiwan University of Science and Technology (NTUST) for their invaluable support in funding and facilitating the process. This research was supported by Institut Sepuluh Nopember under research grant no. 1136/PKS/ITS/2025. Additional funding was provided through the joint research program with NTUST under grant no. 705/PKS/ITS/2025. Authors would also like to thank M. Syahril Hidayatul Azmi for collecting the healthy and Ganodema boninense-infected oil palm leaves from Bangka Island.

Notes and references

1 S. B. Hansen, R. Padfield, K. Syayuti, S. Evers, Z. Zakariah and S. Mastura, *J. Cleaner Prod.*, 2015, **100**, 140–149, DOI: 10.1016/j.jclepro.2015.03.051.
2 Ditjenbun, in *Statistik Perkebunan Indonesia*, Kementerian Pertanian, Jakarta, 2018, vol. 1, pp. 2–9.
3 R. Hushiarian, N. A. Yusof and S. W. Dutse, *SpringerPlus*, 2013, **2**, 555, DOI: 10.1186/2193-1801-2-555.
4 A. Abubakar, M. Y. Ishak, A. A. Bakar and M. K. Uddin, *Environ. Sustainability*, 2022, **5**, 289–303, DOI: 10.1007/s42398-022-00244-7.
5 R. R. M. Paterson, *AIMS Environ. Sci.*, 2020, **7**(5), 366–379, DOI: 10.3934/environsci.2020024.
6 Y. W. Khoo and K. P. Chong, *Front. Plant Sci.*, 2023, **14**, 1156869, DOI: 10.3389/fpls.2023.1156869.
7 L. Zakaria, H. Kulaveraasingham, T. S. Guan, F. Abdullah and H. Y. Wan, *Asia Pac. J. Mol. Biol. Biotechnol.*, 2005, **13**(1), 23–34.
8 A. Z. Madihah, A. S. Idris and A. R. Rafidah, *Afr. J. Biotechnol.*, 2014, **13**(34), 3455–3463, DOI: 10.5897/ajb2013.13604.
9 L. Zakaria, *Plant Dis.*, 2023, **107**, 603–615, DOI: 10.1094/PDIS-02-22-0358-FE.

10 C. A. T. Tee, Y. X. Teoh, P. L. Yee, B. C. Tan and K. W. Lai, *IEEE Access*, 2021, **9**, 105776–105787, DOI: 10.1109/ACCESS.2021.3098307.
11 B. Dalkıran, C. Kaçar, E. Can, P. E. Erden and E. Kılıç, *Monatsh. Chem.*, 2020, **151**, 1773–1783, DOI: 10.1007/s00706-020-02707-1.
12 S. A. Nusaibah, A. Siti Nor Akmar, A. S. Idris, M. Sariah and Z. Mohamad Pauzi, *Plant Physiol. Biochem.*, 2016, **109**, 156–165.
13 N. Rahmat, N. A. Yusof, A. Isha, W. Mui-Yun, R. Hushiarian and F. S. Akanbi, *IEEE Sens. J.*, 2020, **20**(22), 13253–13261, DOI: 10.1109/JSEN.2020.3006537.
14 M. S. Ibrahim, I. A. Seman, M. H. Rusli, M. A. J. Izzuddin, N. Kamarudin, K. Hashim and Z. A. Manaf, *J. Oil Palm Res.*, 2020, **32**(2), 237–244, DOI: 10.21894/jopr.2020.0024.
15 R. R. Suresh, M. Lakshmanakumar, J. B. B. Arockia Jayalatha, K. S. Rajan, S. Sethuraman, U. M. Krishnan and J. B. B. Rayappan, *J. Mater. Sci.*, 2021, **56**, 8951–9006, DOI: 10.1007/s10853-020-05499-1.
16 G. Paimard, E. Ghasali and M. Baeza, *Chemosensors*, 2023, **11**(2), 113, DOI: 10.3390/chemosensors11020113.
17 R. M. Silva, A. D. da Silva, J. R. Camargo, B. S. de Castro, L. M. Meireles, P. S. Silva, B. C. Janegitz and T. A. Silva, *Biosensors*, 2023, **13**(4), 453, DOI: 10.3390/bios13040453.
18 M. Li, Y. T. Li, D. W. Li and Y. T. Long, *Anal. Chim. Acta*, 2012, **734**, 31–44, DOI: 10.1016/j.aca.2012.05.018.
19 S. Cinti, F. Arduini, M. Carbone, L. Sansone, I. Cacciotti, D. Moscone and G. Palleschi, *Electroanalysis*, 2015, **27**(9), 2230–2238, DOI: 10.1002/elan.201500168.
20 D. A. G. Araújo, J. R. Camargo, L. A. Pradela-Filho, A. P. Lima, R. A. A. Muñoz, R. M. Takeuchi, B. C. Janegitz and A. L. Santos, *Microchem. J.*, 2020, **158**, 105297, DOI: 10.1016/j.microc.2020.105297.
21 S. H. Aboutalebi, A. T. Chidembo, M. Salari, K. Konstantinov, D. Wexler, H. Kun Liu and S. Xue Dou, *Energy Environ. Sci.*, 2011, **4**, 1855–1865, DOI: 10.1039/c1ee01039e.
22 S. A. Fowotade, N. A. Yusof, J. Abdullah, Y. Sulaiman and S. F. Abd Rahman, *Sens. Biosens. Res.*, 2019, **23**, 100274, DOI: 10.1016/j.sbsr.2019.100274.
23 B. B. RasulKhan, P. Periakaruppan, S. K. Ponnaiah, G. Venkatachalam and B. Jeyaprabha, *J. Cluster Sci.*, 2021, **32**, 135–144, DOI: 10.1007/s10876-020-01770-2.
24 Y. H. Chen, R. Kirankumar, C. L. Kao and P. Y. Chen, *Electrochim. Acta*, 2016, **205**, 124–131, DOI: 10.1016/j.electacta.2016.04.111.
25 E. Bernalte, C. Marín-Sánchez, E. Pinilla-Gil and C. M. A. Brett, *J. Electroanal. Chem.*, 2013, **709**, 70–76, DOI: 10.1016/j.jelechem.2013.09.007.
26 S. Chen, R. Yuan, Y. Chai and F. Hu, *Microchim. Acta*, 2013, **180**, 15–32, DOI: 10.1007/s00604-012-0904-4.
27 P. Wang, Z. G. Liu, X. Chen, F. L. Meng, J. H. Liu and X. J. Huang, *J. Mater. Chem. A*, 2013, **1**, 9189–9195, DOI: 10.1039/c3ta11155e.
28 N. A. S. Khairi, N. A. Yusof, J. Abdullah, I. A. Seman, N. Ithnin and S. F. A. Rahman, *IEEE Sens. J.*, 2024, **24**(7), 9341–9352, DOI: 10.1109/JSEN.2024.3366953.
29 B. Wiley, Y. Sun and Y. Xia, *Acc. Chem. Res.*, 2007, **40**(10), 1067–1076, DOI: 10.1021/ar7000974.
30 A. Dewi, S. Eka Putri and P. Salempa, *J. Chem.*, 2020, **2**(1), 10–16, DOI: 10.34312/jambchem.v2i1.5024.
31 A. F. Putra, A. S. Ningrum, S. Suyanto, V. M. Pratiwi, M. Y. H. Widianto, I. Irkham, W. T. Wahyuni, I. Rahmawati, F.-M. Wang, C.-H. Huang and R. A. Wahyuono, *ADMET DMPK*, 2025, **13**(4), 2833, DOI: 10.5599/admet.2833.
32 W. T. Wahyuni, B. R. Putra, R. Heryanto, E. Rohaeti, D. H. Y. Yanto and A. Fauzi, *Int. J. Electrochem. Sci.*, 2021, **16**(2), 210221, DOI: 10.20964/2021.02.36.
33 B. B. Rasulkhan, S. K. Ponnaiah, P. Periakaruppan, G. Venkatachalam and J. Balasubramanian, *New J. Chem.*, 2020, **44**, 18149–18156, DOI: 10.1039/d0nj04252h.
34 A. B. D. Nandiyanto, R. Oktiani and R. Ragadhita, *Indones. J. Sci. Technol.*, 2019, **4**(1), 97–118, DOI: 10.17509/ijost.v4i1.15806.
35 L. Morsch, S. Farmer and K. Cunningham, in *Organic Chemistry, LibreTexts*, 2022, ch.12, pp. 1–10.
36 E. Gharibshahi, E. Saion, A. Ashraf and L. Gharibshahi, *Appl. Radiat. Isot.*, 2017, **130**, 211–217, DOI: 10.1016/j.apradiso.2017.09.012.
37 L. Guo, L. Mao, K. Huang and H. Liu, *J. Mater. Sci.*, 2017, **52**, 10738–10750, DOI: 10.1007/s10853-017-1181-8.
38 N. Viet Long, M. Ohtaki, M. Yuasa, S. Yoshida, T. Kuragaki, C. Minh Thi and M. Nogami, *J. Nanomater.*, 2013, 793125, DOI: 10.1155/2013/793125.
39 P. Sathish Kumar, P. Prakash, A. Srinivasan and C. Karuppiah, *J. Power Sources*, 2021, **482**, 228892, DOI: 10.1016/j.jpowsour.2020.228892.
40 F. T. Johra, J. W. Lee and W. G. Jung, *J. Ind. Eng. Chem.*, 2014, **20**(5), 2883–2887, DOI: 10.1016/j.jiec.2013.11.022.
41 P. Tavlarakis, J. J. Urban and N. Snow, *J. Chromatogr. Sci.*, 2011, **49**(6), 457–462, DOI: 10.1093/chrsci/49.6.457.
42 M. Harada and H. Einaga, *Langmuir*, 2006, **22**(5), 2371–2377, DOI: 10.1021/la052378m.
43 T. P. Durrett and R. Welti, *J. Biol. Chem.*, 2021, **296**, 100802, DOI: 10.1016/j.jbc.2021.100802.
44 K. Gutbrod, J. Romer and P. Dörmann, *Prog. Lipid Res.*, 2019, **74**, 1–17, DOI: 10.1016/j.plipres.2019.01.002.
45 H. Deka and M. D. Saikia, *Colloids Surf., A*, 2015, **469**, 51–59, DOI: 10.1016/j.colsurfa.2015.01.007.
46 S. I. Aboobucker and W. P. Suza, *Front. Plant Sci.*, 2019, **10**, 354, DOI: 10.3389/fpls.2019.00354.
47 F. S. Akanbi, N. A. Yusof, J. Abdullah, Y. Sulaiman and R. Hushiarian, *Sensors*, 2017, **17**(7), 1538, DOI: 10.3390/s17071538.
48 J. Liu, Y. Xu, S. Liu, S. Yu, Z. Yu and S. S. Low, *Biosensors*, 2022, **12**(7), 494, DOI: 10.3390/bios12070494.